

---

# Visualizing the PHATE of Neural Networks

---

**Scott Gigante**

Comp. Biol. and Bioinf. Program  
Yale University  
New Haven, CT 06511  
scott.gigante@yale.edu

**Adam S. Charles**

Princeton Neuroscience Institute  
Princeton University  
Princeton, NJ, 08544  
adamsc@princeton.edu

**Smita Krishnaswamy**

Depts. of Genetics and Computer Science  
Yale University  
New Haven, CT 06520  
smita.krishnaswamy@yale.edu

**Gal Mishne**

Halicioğlu Data Science Institute  
University of California, San Diego  
La Jolla, CA 92093  
gmishne@ucsd.edu

## Abstract

Understanding why and how certain neural networks outperform others is key to guiding future development of network architectures and optimization methods. To this end, we introduce a novel visualization algorithm that reveals the internal geometry of such networks: Multislice PHATE (M-PHATE), the first method designed explicitly to visualize how a neural network’s hidden representations of data evolve throughout the course of training. We demonstrate that our visualization provides intuitive, detailed summaries of the learning dynamics beyond simple global measures (i.e., validation loss and accuracy), without the need to access validation data. Furthermore, M-PHATE better captures both the dynamics and community structure of the hidden units as compared to visualization based on standard dimensionality reduction methods (e.g., ISOMAP, t-SNE). We demonstrate M-PHATE with two vignettes: continual learning and generalization. In the former, the M-PHATE visualizations display the mechanism of “catastrophic forgetting” which is a major challenge for learning in task-switching contexts. In the latter, our visualizations reveal how increased heterogeneity among hidden units correlates with improved generalization performance. An implementation of M-PHATE, along with scripts to reproduce the figures in this paper, is available at <https://github.com/scottgigante/M-PHATE>.

## 1 Introduction

Despite their massive increase in popularity in recent years, deep networks are still regarded as opaque and difficult to interpret or analyze. Understanding how and why certain neural networks perform better than others remains an art. The design of neural networks and their training: choice of architectures, regularization, activation functions, and hyperparameters, while informed by theory and prior work, is often driven by intuition and tuned manually [1]. The combination of these intuition-driven selections and long training times even on high-performance hardware (e.g., 3 weeks on 8 GPUs for the popular ResNet-200 network for image classification), means that the combinatorial task of testing all possible choices is impossible, and must be guided by more principled evaluations and explorations.

A natural and widely used measure of evaluation for the difference between network architectures and optimizers is the validation loss. In some situations, the validation loss lacks a clearly defined global meaning, i.e., when the loss function itself is learned, and other evaluations are required [2, 3]. While

such scores are useful for ranking models on the basis of performance, they crucially do not explain why one model outperforms another. To provide additional insight, visualization tools have been employed, for example to analyze the “loss landscape” of a network. Specifically, these visualizations depict how architectural choices modify the smoothness of local minima [4, 5] — a quality assumed to be related to generalization abilities.

Local minima smoothness, however, is only one possible correlate of performance. Another internal quality that can be quantified is the hidden representations of inputs provided by the hidden unit activations. The multi-layered hidden representations of data are, in effect, the single most important feature distinguishing neural networks from classical machine learning techniques in generalization [6–10]. We can view the changes in representation by stochastic gradient descent as a dynamical system evolving from its random initialization to a converged low-energy state. Observing the progression of this dynamical system gives more insight into the learning process than simply observing it at a single point in time (e.g., after convergence.) In this paper, we contribute a novel method of inspecting a neural network’s learning: we visualize the evolution of the network’s hidden representation during training to isolate key qualities predictive of improved network performance.

Analyzing extremely high-dimensional objects such as deep neural networks requires methods that can reduce these large structures into more manageable representations that are efficient to manipulate and visualize. Dimensionality reduction is a class of machine learning techniques which aim to reduce the number of variables under consideration in high-dimensional data while maintaining the structure of a dataset. There exist a wide array of dimensionality reduction techniques designed specifically for visualization, which aim specifically to capture the structure of a dataset in two or three dimensions for the purposes of human interpretation, e.g., MDS [11], t-SNE [12], and Isomap [13]. In this paper, we employ PHATE [14], a kernel-based dimensionality reduction method designed specifically for visualization which uses multidimensional scaling (MDS) [11] to effectively embed the diffusion geometry [15] of a dataset in two or three dimensions.

In order to visualize the evolution of the network’s hidden representation, we take advantage of the longitudinal nature of the data; we have in effect many observations of an evolving dynamical system, which lends itself well to building a graph from the data connecting observations across different points in time. We construct a weighted multislice graph (where a “slice” refers to the network state at a fixed point in time) by creating connections between hidden representations obtained from a single unit across multiple epochs, and from multiple units within the same epoch. A pairwise affinity kernel on this graph reflects the similarity between hidden units and their evolution over time. This kernel is then dimensionality reduced with PHATE and visualized in two dimensions.

The main contributions of this paper are as follows. We present Multislice PHATE (M-PHATE), which combines a novel multislice kernel construction with the PHATE visualization [14]. Our kernel captures the dynamics of an evolving graph structure, that when visualized, gives unique intuition about the evolution of a neural network over the course of training and re-training. We compare M-PHATE to other dimensionality reduction techniques, showing that the combined construction of the multislice kernel and the use of PHATE provide significant improvements to visualization. In two vignettes, we demonstrate the use M-PHATE on established training tasks and learning methods in continual learning, and in regularization techniques commonly used to improve generalization performance. These examples draw insight into the reasons certain methods and architectures outperform others, and demonstrate how visualizing the hidden units of a network with M-PHATE provides additional information to a deep learning practitioner over classical metrics such as validation loss and accuracy, all without the need to access validation data.

## 2 Background

Diffusion maps (DMs) [15] is an important nonlinear dimensionality reduction method that has been used to extract complex relationships between high-dimensional data [16–22]. PHATE [14] aims to optimize diffusion maps for data visualization. We briefly review the two approaches.

Given a high-dimensional dataset  $\{x_i\}$ , DMs operate on a pairwise similarity matrix  $\mathbf{W}$  (e.g., computed via a Gaussian kernel  $\mathbf{W}(x_i, x_j) = \exp\{-\|x_i - x_j\|^2/\epsilon\}$ ). and return an embedding of the data in a low-dimensional Euclidean space. To compute this embedding, the rows of  $\mathbf{W}$  are normalized by  $\mathbf{P} = \mathbf{D}^{-1}\mathbf{W}$ , where  $\mathbf{D}_{ii} = \sum_j \mathbf{W}_{ij}$ . The resulting matrix  $\mathbf{P}$  can be interpreted as the transition matrix of a Markov chain over the dataset and powers of the matrix,  $\mathbf{P}^t$ , represents running

the Markov chain forward  $t$  steps. The matrix  $\mathbf{P}$  thus has a complete sequence of bi-orthogonal left and right eigenvectors  $\phi_i, \psi_i$ , respectively, and a corresponding sequence of eigenvalues  $1 = \lambda_0 \geq |\lambda_1| \geq |\lambda_2| \geq \dots$ . Due to the fast spectrum decay of  $\{\lambda_l\}$ , we can obtain a low-dimensional representation of the data using only the top  $\ell$  eigenvectors. Diffusion maps, defined as  $\Psi_t(x) = (\lambda_1^t \psi_1(x), \lambda_2^t \psi_2(x), \dots, \lambda_\ell^t \psi_\ell(x))$ , embeds the data points into a Euclidean space  $\mathbb{R}^\ell$  where the Euclidean distance approximates the diffusion distance:

$$\mathbf{D}_t^2(x_i, x_j) = \sum_{x_k} \frac{(p_t(x_i, x_k) - p_t(x_j, x_k))^2}{\phi_0(x_k)} \approx \|\Psi_t(x_i) - \Psi_t(x_j)\|_2^2$$

Note that  $\psi_0$  is neglected because it is a constant vector.

To enable successful data visualization, a method must reduce the dimensionality to two or three dimensions; diffusion maps, however, reduces only to the intrinsic dimensionality of the data, which may be much higher. Thus, to calculate a 2D or 3D representation of the data, PHATE applies MDS [11] to the *informational distance* between rows  $i$  and  $j$  of the diffusion kernel  $\mathbf{P}^t$  defined as

$$\Phi_t(i, j) = \|\log \mathbf{P}^t(i) - \log \mathbf{P}^t(j)\|_2$$

where  $t$  is selected automatically as the knee point of the Von Neumann Entropy of the diffusion operator. For further details, see Moon et al. [14].

## 2.1 Related work

We consider the evolving state of a neural network’s hidden units as a dynamical system which can be represented as a *multislice graph* on which we construct a pairwise affinity kernel. Such a kernel considers both similarities between hidden units in the same epoch or time-slice (denoted *intraslice* similarities) and similarities of a hidden unit to itself across different time-slices (denoted *interslice* similarities). The concept of constructing a graph for data changing over time is motivated by prior work both in harmonic analysis [20, 23–25, 22] and network science [26]. For example, Coifman and Hirn [20] suggest an algorithm for jointly analyzing DMs built over data points that are changing over time by aligning the separately constructed DMs, while Mucha et al. [26] suggest an algorithm for community detection in multislice networks by connecting each node in one network slice to itself in other slices, with identical *fixed weights* for all intraslice connections. In both cases, such techniques are designed to detect changes in intraslice dynamics over time, yet interslice dynamics are not incorporated into the model.

## 3 Multiscale PHATE

### 3.1 Preliminaries

Let  $F$  be a neural network with a total of  $m$  hidden units applied to  $d$ -dimensional input data. Let  $F_i : \mathbb{R}^d \rightarrow \mathbb{R}$  be the activation of the  $i$ th hidden unit of  $F$ , and  $F^{(\tau)}$  be the representation of the network after being trained for  $\tau \in \{1, \dots, n\}$  epochs on training data  $X$  sampled from a dataset  $\mathcal{X}$ .

A natural feature space for the hidden units of  $F$  is the activations of the units with respect to the input data. Let  $Y \subset \mathcal{X}$  be a representative sample of  $p \ll |X|$  points. (In this paper, we use points not used in training; however, this is not necessary. Further discussion of this is given in Section S2.) Let  $Y_k$  be the  $k$ th sample in  $Y$ . We use the hidden unit activations  $F(Y)$  to compute a shared feature space of dimension  $p$  for the hidden units. We can then calculate similarities between units from all layers. Note that one may instead consider the hidden units’ learned parameters (e.g. weight matrices and bias terms); however, these are not suitable for our purposes as they are not necessarily the same shape between hidden layers, and additionally the parameters may contain information not relevant to the data (for example, in dimensions of  $\mathcal{X}$  containing no relevant information.)

We denote the *time trace*  $\mathbf{T}$  of the network as a  $n \times m \times p$  tensor containing the activations at each epoch  $\tau$  of each hidden unit  $F_i$  with respect to each sample  $Y_k \in Y$ . We note that in practice, the major driver of variation in  $\mathbf{T}$  is the bias term contributing a fixed value to the activation of each hidden unit. Further, we note that the absolute values of the differences in activation of a hidden unit are not strictly meaningful, since any differences in activation can simply be magnified by a larger

kernel weight in the following layer. Therefore, to calculate more meaningful similarities, we first  $z$ -score the activations of each hidden unit at each epoch  $\tau$

$$\mathbf{T}(\tau, i, k) = \frac{F_i^{(\tau)}(Y_k) - \frac{1}{p} \sum_{\ell} F_i^{(\tau)}(Y_{\ell})}{\sqrt{\text{Var}_{\ell} F_i^{(\tau)}(Y_{\ell})}}.$$

### 3.2 Multislice Kernel

The time trace gives us a natural substrate from which to construct a visualization of the network’s evolution. We construct a kernel over  $\mathbf{T}$  utilizing our prior knowledge of the temporal aspect of  $\mathbf{T}$  to capture its dynamics. Let  $\mathbf{K}$  be a  $nm \times nm$  kernel matrix between all hidden units at all epochs (the  $(\tau m + j)$ th row or column of  $\mathbf{K}$  refers to  $j$ -th unit at epoch  $\tau$ ). We henceforth refer to the  $(\tau m + j)$ th row of  $\mathbf{K}$  as  $\mathbf{K}((\tau, j), :)$  and the  $(\tau m + j)$ th column of  $\mathbf{K}$  as  $\mathbf{K}(:, (\tau, j))$ .

To capture both the evolution of a hidden unit throughout training as well as its community structure with respect to other hidden units, we construct a multislice kernel matrix which reflects both affinities between hidden units  $i$  and  $j$  in the same epoch  $\tau$ , or intraslice affinities

$$\mathbf{K}_{\text{intraslice}}^{(\tau)}(i, j) = \exp\left(-\|\mathbf{T}(\tau, i) - \mathbf{T}(\tau, j)\|_2^{\alpha} / \sigma_{(\tau, i)}^{\alpha}\right)$$

as well as affinities between a hidden unit  $i$  and itself at different epochs, or interslice affinities

$$\mathbf{K}_{\text{interslice}}^{(i)}(\tau, \nu) = \exp\left(-\|\mathbf{T}(\tau, i) - \mathbf{T}(\nu, i)\|_2^2 / \epsilon^2\right)$$

where  $\sigma_{(\tau, i)}$  is the intraslice bandwidth for unit  $i$  at epoch  $\tau$ ,  $\epsilon$  is the fixed intraslice bandwidth, and  $\alpha$  is the adaptive bandwidth decay parameter.

In order to maintain connectivity while increasing robustness to parameter selection for the intraslice affinities  $\mathbf{K}_{\text{intraslice}}^{(\tau)}$ , we use an adaptive-bandwidth Gaussian kernel (termed the *alpha-decay kernel* [14]), with bandwidth  $\sigma_{(\tau, i)}$  set to be the distance of unit  $i$  at epoch  $\tau$  to its  $k$ th nearest neighbor across units at that epoch:  $\sigma_{(\tau, i)} = d_k(\mathbf{T}(\tau, i), \mathbf{T}(\tau, :))$ , where  $d_k(x, X)$  denotes the  $L_2$  distance from  $x$  to its  $k$ th nearest neighbor in  $X$ . Note that the use of the adaptive bandwidth means that the kernel is not symmetric and will require symmetrization. In order to allow the kernel to represent changing dynamics of units over the course of learning, we use a fixed-bandwidth Gaussian kernel in the interslice affinities  $\mathbf{K}_{\text{interslice}}^{(i)}$ , where  $\epsilon$  is the average across all epochs and all units of the distance of unit  $i$  at epoch  $\tau$  to its  $k$ th nearest neighbor among the set consisting of the same unit  $i$  at all other epochs  $\epsilon = \frac{1}{nm} \sum_{\tau=1}^n \sum_{i=1}^m d_{\kappa}(\mathbf{T}(\tau, i), \mathbf{T}(:, i))$ .

Finally, the multislice kernel matrix contains one row and column for each unit at each epoch, such that the intraslice affinities form a block diagonal matrix and the interslice affinities form off-diagonal blocks composed of diagonal matrices (see Figures S1 and S2 for a diagram):

$$\mathbf{K}((\tau, i), (\nu, j)) = \begin{cases} \mathbf{K}_{\text{intraslice}}^{(\tau)}(i, j), & \text{if } \tau = \nu; \\ \mathbf{K}_{\text{interslice}}^{(i)}(\tau, \nu), & \text{if } i = j; \\ 0, & \text{otherwise.} \end{cases}$$

We symmetrize this kernel as  $\mathbf{K}' = \frac{1}{2}(\mathbf{K} + \mathbf{K}^T)$ , and row normalize it to obtain  $\mathbf{P} = \mathbf{D}^{-1}\mathbf{K}'$ , which represents a random walk over all units across all epochs, where propagating from  $(\tau, i)$  to  $(\nu, j)$  is conditional on the transition probabilities between epochs  $\tau$  and  $\nu$ . PHATE [14] is applied to  $\mathbf{P}$  to visualize the time trace  $\mathbf{T}$  in two or three dimensions.

## 4 Results

### 4.1 Example visualization

To demonstrate our visualization, we train a feedforward neural network with 3 layers of 64 hidden units to classify digits in MNIST [27]. The visualization is built on the time trace  $T$  evaluated on the network over a single round of training that lasted 300 epochs and reached 96% validation accuracy.

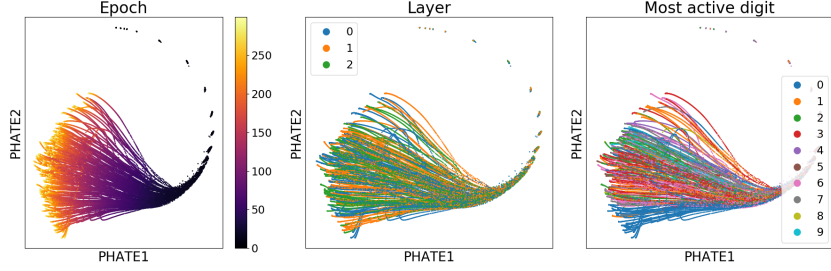


Figure 1: Visualization of a simple 3-layer MLP trained on MNIST with M-PHATE. Visualization is colored by epoch (left), hidden layer (center), and most active digit for each unit (right).

We visualize the network using M-PHATE (Fig. 1) colored by epoch, hidden layer and the digit for which examples of that digit most strongly activate the hidden unit. The embedding is clearly organized longitudinally by epoch, with larger jumps between early epochs and gradually smaller steps as the network converges. Additionally, increased structure emerges in the latter epochs as the network learns meaningful representations of the digits, and groups of neurons activating on the same digits begin to co-localize. Neurons of different layers frequently co-localize, showing that our visualization allows meaningful comparison of hidden units in different hidden layers.

#### 4.2 Comparison to other visualization methods

To evaluate the quality of the M-PHATE visualization, we compare to three established visualization methods: diffusion maps, t-SNE and ISOMAP. We also compare our multislice kernel to the standard formalism of these visualization techniques, by computing pairwise distances or affinities between all units at all time points without taking into account the multislice nature of the data.

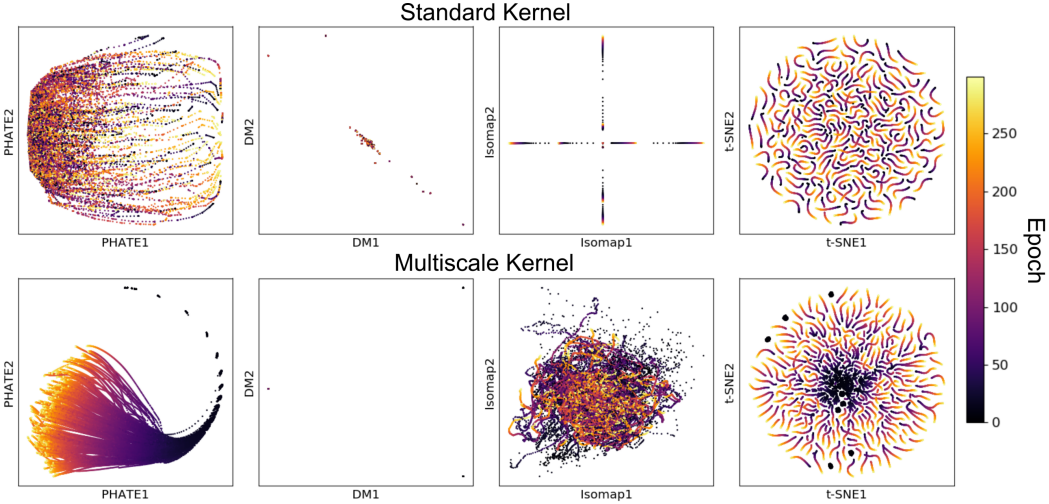


Figure 2: Comparison of standard application of visualization algorithms. Each point represents a hidden unit at a given epoch during training and is colored by the epoch.

Figure 2 shows the standard and multislice visualizations for all four dimensionality reduction techniques of the network in Section 4.1. For implementation details, see Section S3. Only the Multislice PHATE visualization reveals any meaningful evolution of the neural network over time. To quantify the quality of the visualization, we compare both interslice and intraslice neighborhoods in the embedding to the equivalent neighborhoods in the original data. Specifically, for a visualization  $V$  we define the intraslice neighborhood preservation of a point  $V(t, i) \in V$  as

$$\frac{1}{|k|} \left| \mathcal{N}_{V(\tau,:)}^k(V(\tau, i)) \cap \mathcal{N}_{T(\tau,:)}^k(T(\tau, i)) \right|$$

Table 1: Neighborhood preservation of visualization methods applied to a FFNN classifying MNIST.

	Multislice				Standard			
	PHATE	DM	Isomap	t-SNE	PHATE	DM	Isomap	t-SNE
Intraslice, $k = 10$	<b>0.26</b>	0.19	0.11	0.13	0.05	0.09	0.06	0.06
Interslice, $k = 10$	0.95	0.58	0.79	0.91	0.47	0.44	0.68	<b>0.96</b>
Intraslice, $k = 40$	<b>0.45</b>	0.36	0.25	0.26	0.21	0.26	0.22	0.22
Interslice, $k = 40$	0.93	0.75	0.78	0.92	0.67	0.54	0.70	<b>0.94</b>
Loss Correlation	<b>0.81</b>	0.61	0.61	0.33	0.25	0.13	0.47	-0.04

and the interslice neighborhood preservation of  $V(t, i)$  as

$$\frac{1}{|k|} \left| \mathcal{N}_{V(:,i)}^k(V(\tau, j)) \cap \mathcal{N}_{T(:,i)}^k(T(\tau, i)) \right|$$

where  $\mathcal{N}_X^k(x)$  denotes the  $k$  nearest neighbors of  $x$  in  $X$ . We also calculate the Spearman correlation of the rate of change of each hidden unit with the rate of change of the validation loss to quantify the fidelity of the visualization to the diminishing rate of convergence towards the end of training.

M-PHATE achieves the best neighborhood preservation on all measures except the interslice neighborhood preservation, in which it performs on-par with standard t-SNE. Additionally, the multislice kernel construction outperforms the corresponding standard kernel construction for all methods and all measures, except again in the case of t-SNE for interslice neighborhood preservation. M-PHATE also has the highest correlation with change in loss, making it the most faithful display of network convergence.

### 4.3 Continual learning

An ongoing challenge in artificial intelligence is in making a single model perform well on many tasks independently. The capacity to succeed at dynamically changing tasks is often considered a hallmark of genuine intelligence, and is thus crucial to develop in artificial intelligence [28]. Continual learning is one attempt at achieving this goal sequentially training a single network on different tasks with the aim of instilling the network with new abilities as data becomes available.

To assess networks designed for continual learning tasks, a set of training baselines have been proposed. Hsu et al. [29] define three types of continual learning scenarios for classification: incremental task learning, in which a separate binary output layer is used for each task; incremental domain learning, in which a single binary output layer performs all tasks; and incremental class learning, in which a single 10-unit output layer is used, with each pair of output units used for just a single task. Further details are given in Section S4.

We implemented a 2-layer MLP with 400 units in each hidden layer to perform incremental, domain and class learning tasks using three described baselines: standard training with Adagrad [30] and Adam [31], and an experience replay training scheme called Naive Rehearsal [29] in which a small set of training examples from each task are retained and replayed to the network during subsequent tasks. Each network was trained for 4 epochs before switching to the next task. Overall, we find that validation performance is fairly consistent with results reported in Hsu et al. [29], with Naive Rehearsal performing best, followed by Adagrad and Adam. Class learning was the most challenging, followed by domain learning and task learning.

Figure 3 shows M-PHATE visualizations of learning in networks trained in each of three baselines, with network slices taken every 50 batches rather than every epoch for increased resolution. Notably, we observe a stark difference in how structure is preserved over training between networks, which is predictive of task performance. The highest-performing networks all tend to preserve representational structure across changing tasks. On the other hand, networks trained with Adam — the worst performing combinations — tend to have a structural “collapse”, or rapid change in connectivity, as the tasks switch, consistent with the rapid change (and eventual increase) in validation loss.

Further, the frequency of neighborhood changes for hidden units throughout training (appearing as a crossing of unit trajectories in the visualization) corresponds to an increase in validation loss; this is due to a change in function of the hidden units, corrupting the intended use of such units

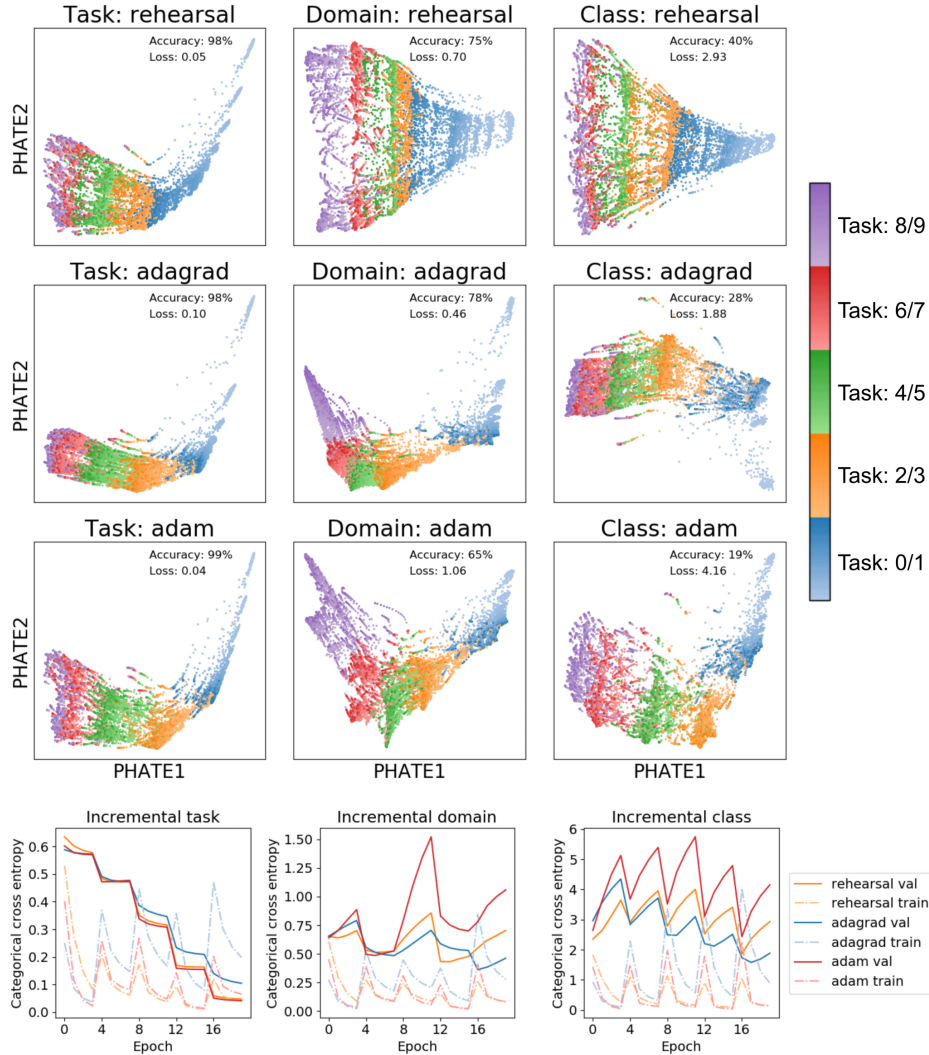


Figure 3: Visualization of a 2 layer MLP trained on Split MNIST for five-task continual learning of binary classification. Training loss and accuracy are reported on the current task. Validation loss and accuracy is reported on a test set consisting of an even number of samples from all tasks. Only 100 neurons are shown for clarity. Full plots are available in Section S4.

for earlier tasks. We quantify this effect by calculating the Adjusted Rand Index (ARI) on cluster assignments computed on the subset of the visualization corresponding to the hidden units pre- and post-task switch, and find that the average ARI is strongly negatively correlated with the network’s final validation loss averaged over all tasks ( $\rho = 0.94$ ).

Looking for such signatures, including rapid changes in hidden unit structure and crossing of unit trajectories, can thus be used to understand the efficiency of continual learning architectures.

#### 4.4 Generalization

Despite being massively overparametrized, neural networks frequently exhibit astounding generalization performance [32, 33]. Recent work has showed that, despite having the capacity to memorize, neural networks tend to learn abstract, generalizable features rather than memorizing each example, and that this behaviour is qualitatively different in gradient descent compared to memorization [34].

Table 2: Adjusted Rand Index of cluster assignments computed on the subset of the PHATE visualization corresponding to the hidden units pre- and post-task switch. ARI is averaged across all four task switches, 6 different choices of clustering parameter (between 3–8 clusters) and 20 random seeds. Loss refers to average validation loss averaged over all tasks after completion of training.

	Task			Domain			Class		
	Rehears.	Adagr.	Adam	Rehears.	Adagr.	Adam	Rehears.	Adagr.	Adam
Val. Loss	0.047	0.104	0.042	0.709	0.462	1.062	2.904	1.884	4.156
ARI	0.741	0.772	0.716	0.719	0.768	0.740	0.614	0.632	0.466

Table 3: Summed variance per epoch of the PHATE visualization is associated with the difference between a network that is memorizing and a network that is generalizing. Memorization error refers to the difference between train loss and validation loss.

	Dropout	Kernel		Vanilla	Activity		Random	
		L1	L2		L1	L2	Labels	Pixels
Memorization	-0.09	0.02	0.03	0.04	0.11	0.12	0.15	0.92
Variance	382	141	50	46	0.47	0.15	0.42	0.03

In order to demonstrate the difference between networks that learn to generalize and networks that learn to memorize, we train a 3-layer MLP with 128 hidden units in each layer to classify MNIST with: no regularization;  $L_1/L_2$  weight regularization;  $L_1/L_2$  activity regularization; and dropout. Additionally, we train the same network to classify MNIST with random labels, as well as to classify images with randomly valued pixels, such networks being examples of pure memorization. Each network was trained for 300 epochs, and the discrepancy between train and validation loss reported.

We note that in Figure 4, the networks with the poorest generalization (i.e. those with greatest divergence between train and validation loss), especially Activity  $L_1$  and Activity  $L_2$ , display less heterogeneity in the visualization. To quantify this, we calculate the sum of the variance for all time slices of each embedding and regress this against the *memorization error* of each network, defined as the discrepancy between train and test loss after 300 epochs (Table 3), achieving a Spearman correlation of  $\rho = -0.98$ .

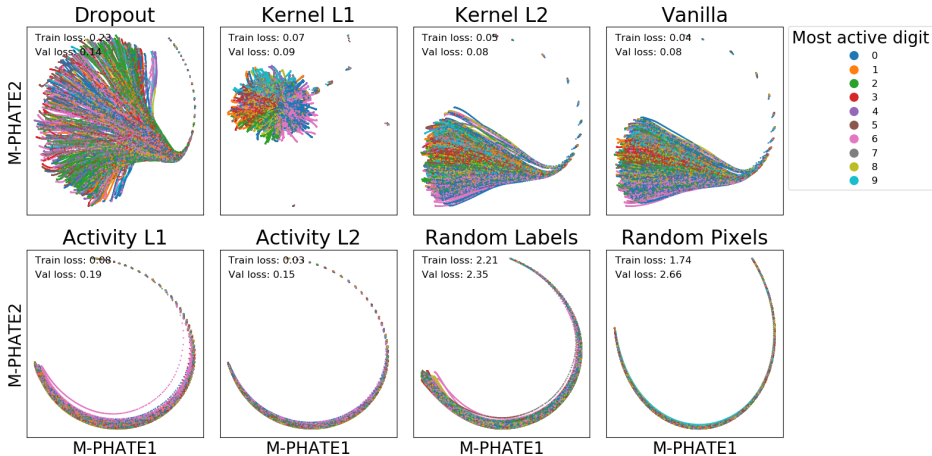


Figure 4: Visualization of a 3-layer MLP trained to classify MNIST with different regularizations or manipulations applied to affect generalization performance.

To understand this phenomenon, we consider the random labels network. In order to memorize random labels, the neural network must hone in on minute differences between images of the same true class in order to classify them differently. Since most images won't satisfy such specific criteria most nodes will not respond to any given image, leading to low activation heterogeneity and



high similarities between hidden units. The M-PHATE visualization clearly exposes this intuition visually, depicting very little difference between these hidden units. Similar intuition can be drawn from the random pixels network, in which the difference between images is purely random. We hypothesize that applying  $L_1$  or  $L_2$  regularization over the activations has a qualitatively similar effect; reducing the variability in activations and effectively over-emphasizing small differences in the hidden representation. This behavior effectively mimics the effects of memorization.

On the other hand, we consider the dropout network, which displays the greatest heterogeneity. Initial intuition evoked the idea that dropout emulates an ensemble method within a single network; by randomly removing units from the network during training, the network learns to combine the output of many sub-networks, each of which is capable of correctly classifying the input Srivastava et al. [35]. M-PHATE visualization of training with dropout recommends a more mechanistic version of this intuition: dropped-out nodes are protected from receiving the exact same gradient signals and diverge to a more expressive representation. The resulting heterogeneity in the network reduces the reliance on small differences between training examples and heightens the network’s capacity to generalize. This intuition falls in line with other theoretical explorations, such as viewing dropout as a form of Bayesian regularization [36] or stochastic gradient descent [37] and reinforces our understanding of why dropout induces generalization.

We note that while this experiment uses validation data as input to M-PHATE, we have repeated this experiment in Section S2 and show equivalent results. In doing so, we provide a mechanism to understand the generalization performance of a network without requiring access to validation data.

## 5 Conclusion

Here we have introduced a novel approach to examining the process of learning in deep neural networks through a visualization algorithm we call M-PHATE. M-PHATE takes advantage of the dynamic nature of the hidden unit activations over the course of training to provide an interpretable visualization otherwise unattainable with standard visualizations. We demonstrate M-PHATE with two vignettes in continual learning and generalization, drawing conclusions that are not apparent without such a visualization, and providing insight into the performance of networks without necessarily requiring access to validation data. In doing so, we demonstrate the utility of such a visualization to the deep learning practitioner.

## References

- [1] Bobak Shahriari, Kevin Swersky, Ziyu Wang, Ryan P. Adams, and Nando de Freitas. Taking the human out of the loop: A review of bayesian optimization. *Proceedings of the IEEE*, 104(1):148–175, 2016. doi: 10.1109/JPROC.2015.2494218. URL <https://doi.org/10.1109/JPROC.2015.2494218>.
- [2] Tim Salimans, Ian J. Goodfellow, Wojciech Zaremba, Vicki Cheung, Alec Radford, and Xi Chen. Improved techniques for training gans. In *Advances in Neural Information Processing Systems 29: Annual Conference on Neural Information Processing Systems 2016, December 5-10, 2016, Barcelona, Spain*, pages 2226–2234, 2016. URL <http://papers.nips.cc/paper/6125-improved-techniques-for-training-gans>.
- [3] Mario Lucic, Karol Kurach, Marcin Michalski, Sylvain Gelly, and Olivier Bousquet. Are gans created equal? A large-scale study. In *Advances in Neural Information Processing Systems 31: Annual Conference on Neural Information Processing Systems 2018, NeurIPS 2018, 3-8 December 2018, Montréal, Canada.*, pages 698–707, 2018. URL <http://papers.nips.cc/paper/7350-are-gans-created-equal-a-large-scale-study>.
- [4] Ian J. Goodfellow and Oriol Vinyals. Qualitatively characterizing neural network optimization problems. In *3rd International Conference on Learning Representations, ICLR 2015, San Diego, CA, USA, May 7-9, 2015, Conference Track Proceedings*, 2015. URL <http://arxiv.org/abs/1412.6544>.
- [5] Hao Li, Zheng Xu, Gavin Taylor, Christoph Studer, and Tom Goldstein. Visualizing the loss landscape of neural nets. In *Advances in Neural Information Processing Systems 31: Annual*

- Conference on Neural Information Processing Systems 2018, NeurIPS 2018, 3-8 December 2018, Montréal, Canada.*, pages 6391–6401, 2018. URL <http://papers.nips.cc/paper/7875-visualizing-the-loss-landscape-of-neural-nets>.
- [6] Yann LeCun, Yoshua Bengio, and Geoffrey E. Hinton. Deep learning. *Nature*, 521(7553):436–444, 2015. doi: 10.1038/nature14539. URL <https://doi.org/10.1038/nature14539>.
- [7] Yoshua Bengio, Olivier Delalleau, and Nicolas Le Roux. The curse of highly variable functions for local kernel machines. In *Advances in Neural Information Processing Systems 18 [Neural Information Processing Systems, NIPS 2005, December 5-8, 2005, Vancouver, British Columbia, Canada]*, pages 107–114, 2005. URL <http://papers.nips.cc/paper/2810-the-curse-of-highly-variable-functions-for-local-kernel-machines>.
- [8] Yoshua Bengio. Learning deep architectures for AI. *Foundations and Trends in Machine Learning*, 2(1):1–127, 2009. doi: 10.1561/2200000006. URL <https://doi.org/10.1561/2200000006>.
- [9] Guido F. Montúfar and Jason Morton. When does a mixture of products contain a product of mixtures? *SIAM J. Discrete Math.*, 29(1):321–347, 2015. doi: 10.1137/140957081. URL <https://doi.org/10.1137/140957081>.
- [10] Guido F. Montúfar, Razvan Pascanu, KyungHyun Cho, and Yoshua Bengio. On the number of linear regions of deep neural networks. In *Advances in Neural Information Processing Systems 27: Annual Conference on Neural Information Processing Systems 2014, December 8-13 2014, Montreal, Quebec, Canada*, pages 2924–2932, 2014. URL <http://papers.nips.cc/paper/5422-on-the-number-of-linear-regions-of-deep-neural-networks>.
- [11] Trevor F Cox and Michael AA Cox. *Multidimensional scaling*. Chapman and hall/CRC, 2000.
- [12] Laurens van der Maaten and Geoffrey Hinton. Visualizing data using t-sne. *Journal of machine learning research*, 9(Nov):2579–2605, 2008.
- [13] Joshua B Tenenbaum, Vin De Silva, and John C Langford. A global geometric framework for nonlinear dimensionality reduction. *science*, 290(5500):2319–2323, 2000.
- [14] Kevin R Moon, David van Dijk, Zheng Wang, Scott Gigante, Daniel Burkhardt, William Chen, Antonia van den Elzen, Matthew J Hirn, Ronald R Coifman, Natalia B Ivanova, Guy Wolf, and Smita Krishnaswamy. Visualizing transitions and structure for high dimensional data exploration. *bioRxiv*, page 120378, 2017.
- [15] Ronald R Coifman and Stéphane Lafon. Diffusion maps. *Applied and computational harmonic analysis*, 21(1):5–30, 2006.
- [16] J. He, L. Zhang, Q. Wang, and Z. Li. Using diffusion geometric coordinates for hyperspectral imagery representation. *IEEE Geosci. Remote Sens. Letters*, 6(4):767–771, Oct. 2009.
- [17] Zeev Farbman, Raanan Fattal, and Dani Lischinski. Diffusion maps for edge-aware image editing. *ACM Trans. Graph.*, 29(6):145:1–145:10, Dec. 2010.
- [18] Ronen Talmon, Israel Cohen, and Sharon Gannot. Single-channel transient interference suppression with diffusion maps. *IEEE Trans. Audio, Speech Lang. Process.*, 21(1):130–142, Apr. 2012.
- [19] Gal Mishne and Israel Cohen. Multiscale anomaly detection using diffusion maps. *IEEE J. Sel. Topics Signal Process.*, 7:111 – 123, Feb. 2013.
- [20] Ronald R Coifman and Matthew J Hirn. Diffusion maps for changing data. *Applied and computational harmonic analysis*, 36(1):79–107, 2014.
- [21] Gal Mishne, Ronen Talmon, Ron Meir, Jackie Schiller, Maria Lavzin, Uri Dubin, and Ronald R. Coifman. Hierarchical coupled-geometry analysis for neuronal structure and activity pattern discovery. *IEEE Journal of Selected Topics in Signal Processing*, 10(7):1238–1253, Oct 2016. ISSN 1932-4553. doi: 10.1109/JSTSP.2016.2602061.

- [22] Ralf Banisch and Péter Koltai. Understanding the geometry of transport: Diffusion maps for lagrangian trajectory data unravel coherent sets. *Chaos: An Interdisciplinary Journal of Nonlinear Science*, 27(3):035804, 2017. doi: 10.1063/1.4971788. URL <https://doi.org/10.1063/1.4971788>.
- [23] Ofir Lindenbaum, Arie Yeredor, Moshe Salhov, and Amir Averbuch. Multiview diffusion maps. *arXiv preprint arXiv:1508.05550*, 2015.
- [24] Roy R Lederman and Ronen Talmon. Learning the geometry of common latent variables using alternating-diffusion. *Applied and Computational Harmonic Analysis*, 44(3):509–536, 2018.
- [25] Nicholas F Marshall and Matthew J Hirn. Time coupled diffusion maps. *Applied and Computational Harmonic Analysis*, 45(3):709–728, 2018.
- [26] Peter J Mucha, Thomas Richardson, Kevin Macon, Mason A Porter, and Jukka-Pekka Onnela. Community structure in time-dependent, multiscale, and multiplex networks. *Science*, 328(5980):876–878, 2010.
- [27] Yann LeCun, Léon Bottou, Yoshua Bengio, Patrick Haffner, et al. Gradient-based learning applied to document recognition. *Proceedings of the IEEE*, 86(11):2278–2324, 1998.
- [28] German Ignacio Parisi, Ronald Kemker, Jose L. Part, Christopher Kanan, and Stefan Wermter. Continual lifelong learning with neural networks: A review. *Neural Networks*, 113:54–71, 2019. doi: 10.1016/j.neunet.2019.01.012. URL <https://doi.org/10.1016/j.neunet.2019.01.012>.
- [29] Yen-Chang Hsu, Yen-Cheng Liu, and Zsolt Kira. Re-evaluating continual learning scenarios: A categorization and case for strong baselines. *CoRR*, abs/1810.12488, 2018. URL <http://arxiv.org/abs/1810.12488>.
- [30] John C. Duchi, Elad Hazan, and Yoram Singer. Adaptive subgradient methods for online learning and stochastic optimization. *Journal of Machine Learning Research*, 12:2121–2159, 2011. URL <http://dl.acm.org/citation.cfm?id=2021068>.
- [31] Diederik P. Kingma and Jimmy Ba. Adam: A method for stochastic optimization. In *3rd International Conference on Learning Representations, ICLR 2015, San Diego, CA, USA, May 7-9, 2015, Conference Track Proceedings*, 2015. URL <http://arxiv.org/abs/1412.6980>.
- [32] Chiyuan Zhang, Samy Bengio, Moritz Hardt, Benjamin Recht, and Oriol Vinyals. Understanding deep learning requires rethinking generalization. In *5th International Conference on Learning Representations, ICLR 2017, Toulon, France, April 24-26, 2017, Conference Track Proceedings*, 2017. URL <https://openreview.net/forum?id=Sy8gdB9xx>.
- [33] Zeyuan Allen-Zhu, Yuanzhi Li, and Yingyu Liang. Learning and generalization in overparameterized neural networks, going beyond two layers. *CoRR*, abs/1811.04918, 2018. URL <http://arxiv.org/abs/1811.04918>.
- [34] Devansh Arpit, Stanislaw K. Jastrzebski, Nicolas Ballas, David Krueger, Emmanuel Bengio, Maxinder S. Kanwal, Tegan Maharaj, Asja Fischer, Aaron C. Courville, Yoshua Bengio, and Simon Lacoste-Julien. A closer look at memorization in deep networks. In *Proceedings of the 34th International Conference on Machine Learning, ICML 2017, Sydney, NSW, Australia, 6-11 August 2017*, pages 233–242, 2017. URL <http://proceedings.mlr.press/v70/arpit17a.html>.
- [35] Nitish Srivastava, Geoffrey E. Hinton, Alex Krizhevsky, Ilya Sutskever, and Ruslan Salakhutdinov. Dropout: a simple way to prevent neural networks from overfitting. *Journal of Machine Learning Research*, 15(1):1929–1958, 2014. URL <http://dl.acm.org/citation.cfm?id=2670313>.
- [36] Yarín Gal and Zoubin Ghahramani. Dropout as a bayesian approximation: Representing model uncertainty in deep learning. In *international conference on machine learning*, pages 1050–1059, 2016.

- [37] Pierre Baldi and Peter J Sadowski. Understanding dropout. In *Advances in neural information processing systems*, pages 2814–2822, 2013.
- [38] F. Pedregosa, G. Varoquaux, A. Gramfort, V. Michel, B. Thirion, O. Grisel, M. Blondel, P. Prettenhofer, R. Weiss, V. Dubourg, J. Vanderplas, A. Passos, D. Cournapeau, M. Brucher, M. Perrot, and E. Duchesnay. Scikit-learn: Machine learning in Python. *Journal of Machine Learning Research*, 12:2825–2830, 2011.
- [39] François Chollet et al. Keras. <https://keras.io>, 2015.
- [40] Martín Abadi, Paul Barham, Jianmin Chen, Zhifeng Chen, Andy Davis, Jeffrey Dean, Matthieu Devin, Sanjay Ghemawat, Geoffrey Irving, Michael Isard, Manjunath Kudlur, Josh Levenberg, Rajat Monga, Sherry Moore, Derek Gordon Murray, Benoit Steiner, Paul A. Tucker, Vijay Vasudevan, Pete Warden, Martin Wicke, Yuan Yu, and Xiaoqiang Zheng. Tensorflow: A system for large-scale machine learning. In *12th USENIX Symposium on Operating Systems Design and Implementation, OSDI 2016, Savannah, GA, USA, November 2-4, 2016.*, pages 265–283, 2016. URL <https://www.usenix.org/conference/osdi16/technical-sessions/presentation/abadi>.

## S1 Multislice graph construction

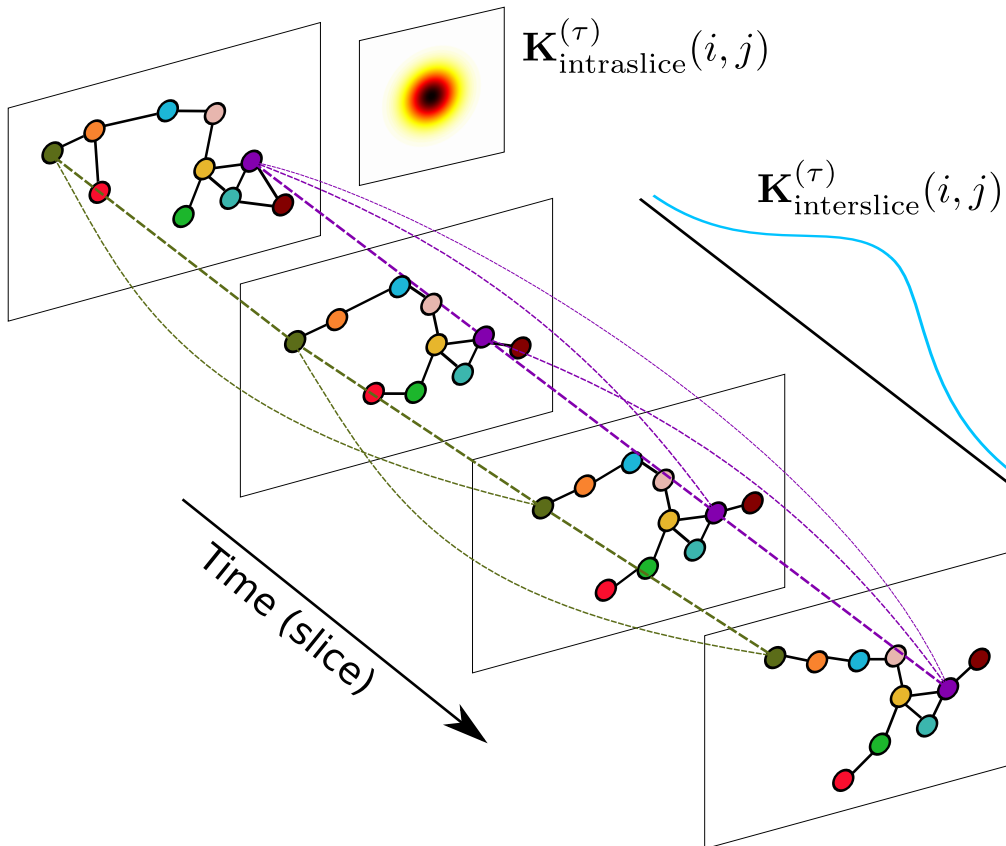


Figure S1: Example schematic of the multislice graph used in M-PHATE. The intra- and interslice kernels represent the similarities between the graph nodes at different time-points, providing PHATE with a time-aware distance to visualize the data with.

In Section 3, we describe a multislice affinity kernel  $K$  built from an *intraslice* kernel, which connects hidden units in the same epoch, and an *interslice* kernel, which connects each hidden unit to itself at different epochs. We further clarify the intuition behind such an affinity kernel in two schematics.

Figure S1 displays a graph of 10 hidden units in a dynamically changing graph structure over the course of four time slices. Each hidden unit’s local neighborhood within its own time slice (its intraslice affinities) changes as the system evolves, with connectivity shown as black lines. Additionally, each hidden unit is connected to itself across different epochs, with strength of these interslice connections (shown as dotted lines) also dependent on similarities (rather than simply a fixed-weight connection).

Figure S2 displays the top left corner of an example of a multislice affinity kernel. The full multislice kernel ( $\mathbf{K}((\tau, i), (v, j))$ , left) is composed on the intraslice kernels placed down the block diagonal ( $\mathbf{K}_{\text{intraslice}}^{(1)}(i, j), \dots, \mathbf{K}_{\text{intraslice}}^{(\tau)}(i, j)$ , middle) and the interslice kernels forming the diagonals of each off-diagonal block ( $K_{\text{interslice}}^{(1)}(\tau, v), \dots, K_{\text{interslice}}^{(i)}(\tau, v)$ , right).

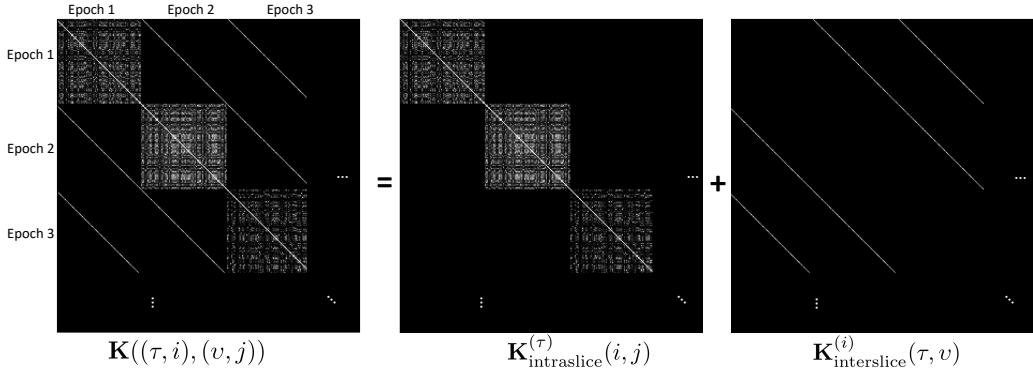


Figure S2: Example schematic of the multislice kernel used in M-PHATE. This kernel is a sum of intraslice and interslice affinities.

## S2 Selection of representative subset $Y$

In Section 3, we state that the representative subset  $Y$  is taken from points not used in training. However, there is no reason why this should be the case. To demonstrate that M-PHATE can be used successfully without accessing data external to the training set, we show in Figure S3 a repetition of the generalization experiment, using only training data to build the visualization. Using the same quantification of variance and memorization as in Section 4.4, we obtain an equally strong correlation (Spearman’s  $\rho = -0.95$ , Table S1). Further, we note that the visualizations are qualitatively very similar to those obtained using training data, indicating that M-PHATE can be used to understand the generalization performance of a network without having access to an external validation set.

## S3 Parameters for visualization methods comparison

In Section 4.2, we compare M-PHATE to Diffusion Maps, t-SNE and Isomap in both a standard and multiscale context. Since t-SNE and Isomap require distance matrices, not affinity matrices, we convert the multislice kernel to geodesic distances by computing the shortest-path over the graph with the distance  $D = -\log K'$ . For standard application of Isomap and t-SNE, we use the default parameters in sklearn [38]. Since diffusion maps can be applied to any symmetric non-negative affinity kernel and does not have a reference implementation, we apply diffusion maps to the adaptive bandwidth kernel built in PHATE.

## S4 Continual Learning

### Continual Learning Schemes

Hsu et al. [29] describe three schemes of continual learning commonly used in the literature.

Incremental *task* learning describes the process of learning shared hidden units for separated output layers for each task; the output units for task  $i$  are therefore protected from gradient signals during

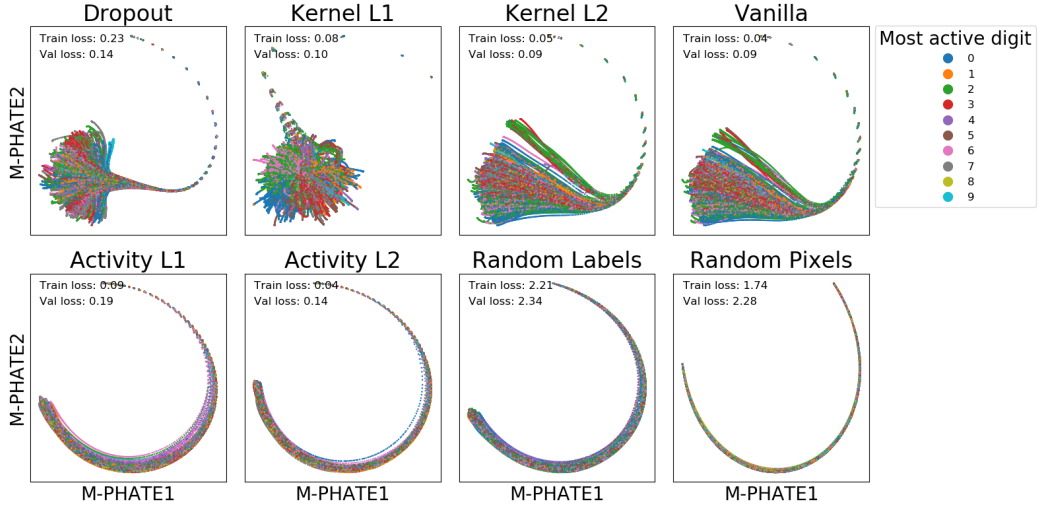


Figure S3: Visualization of a 3-layer MLP trained to classify MNIST with different regularizations or manipulations applied to affect generalization performance, where the visualization is built using only training data.

Table S1: Summed variance per epoch of the PHATE visualization is associated with the difference between a network that is memorizing and a network that is generalizing, where the visualization is built using only training data. Memorization error refers to the difference between train loss and validation loss.

	Dropout	Kernel			Activity		Random	
		L1	L2	Vanilla	L1	L2	Labels	Pixels
Memorization	-0.09	0.02	0.04	0.05	0.10	0.12	0.13	0.53
Variance	59	77	35	28	0.66	0.34	0.37	0.03

the training of task  $j \neq i$ . This is akin to the standard model of transfer learning, in which all but the final layer of a network are copied for a new task, with a fresh output layer attached for the new task.

Incremental *domain* learning describes the process of learning an entirely shared network which learns to perform all tasks separately, but with the same units; in this case the output units for task  $i$  are the same units that are used in task  $j$  and must learn to correctly classify training examples from separate tasks as though they were the same class.

Incremental *class* learning describes the process of learning an entirely shared network which learns to perform all tasks at once, with no knowledge of which task is currently being performed. The network contains separate output units for each task, but must select which output units to use, in contrast to incremental task learning in which the task is specified. This is by far the most difficult setting, since in training any one task, the optimal solution is to never predict the output classes of any other task; this strongly encourages catastrophic forgetting.

Figure S4 demonstrates these three architectures on Split MNIST.

### Network Parameters

The networks in Section 4.3 are trained as follows. Input data is scaled from 0 to 1. All networks consist of a MLP with 2 layers of 400 units with ReLU activation, and a softmax classification output layer. All networks are trained with a batch size of 128, split to batches of 64 new data and 64 rehearsal data in the case of Naive Rehearsal. For the Adam optimizer, we use a learning rate of  $1e^{-5}$ . For the Adagrad optimizer, we use a learning rate of  $1e^{-4}$ . For Naive Rehearsal, we use the Adam optimizer. All networks are built and trained in Keras using a Tensorflow backend.

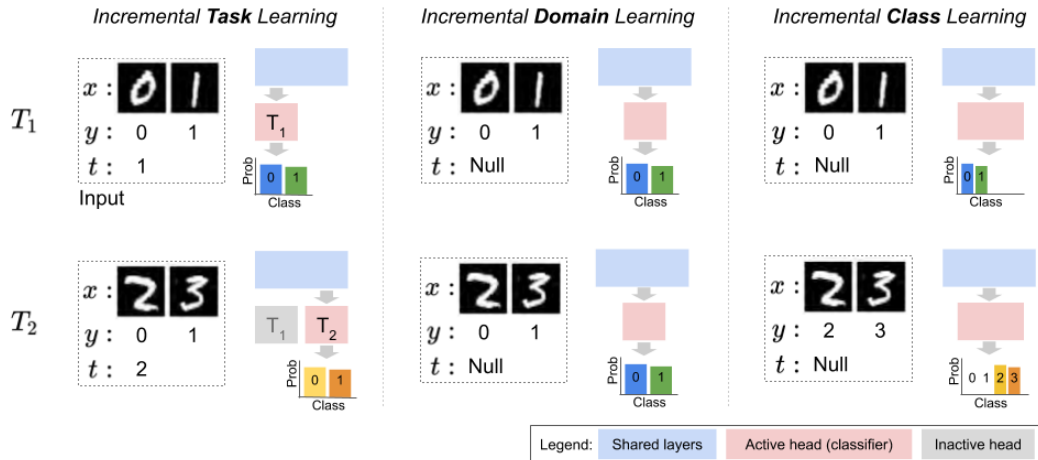


Figure S4: Architectures for incremental learning scenarios. Reproduced with permission from Hsu et al. [29].

## Results

Figure 3 shows the visualizations of the continual learning networks for a subset of 100 hidden units from each layer of the MLP with 2 layers of 400 units. Figures S5 and S6 show the full embedding of layers 1 and 2 respectively. In all cases, the visualizations are computed on all hidden units and subsampled for plotting purposes only.

We note the striking difference between layer 1 and layer 2 in all visualizations. In every case, there is less “structural collapse” (see Section 4.4) in layer 2 than in layer 1. Also, the vertical patterning in layer 2 is perfectly associated with time-slice; that is, in each task (composed of 16 time-slices), the majority of change in hidden representations in layer 2 occurs within the first two or three time slices. On the other hand, layer 1 continues to change throughout the task.

## S5 Generalization

### Network Parameters

The networks in Section 4.4 are trained as follows. Input data is scaled from 0 to 1. All networks consist of a MLP with 3 layers of 128 units with Leaky ReLU activation with  $\alpha = 0.1$ , and a softmax classification output layer. All networks are trained with a batch size of 256 with the Adam optimizer and a learning rate of  $1e^{-5}$ . All regularizations are applied with a weight of  $1e^{-4}$ . Dropout is applied with  $p = 0.5$ . For the scrambled network, we randomly permute the output labels of the training data, leaving the validation data intact. All networks are built and trained in Keras [39] using a Tensorflow [40] backend.

### S6 M-PHATE parameters

All multislice graphs are built with  $k = 2$ ,  $\alpha = 5$  and  $\kappa = 25$ . We apply PHATE on the multislice affinity matrix with PHATE parameters  $\gamma = 0$  and  $n\_landmark = 3000$ , and use the automatically selected parameter of  $t$  provided by the PHATE algorithm.

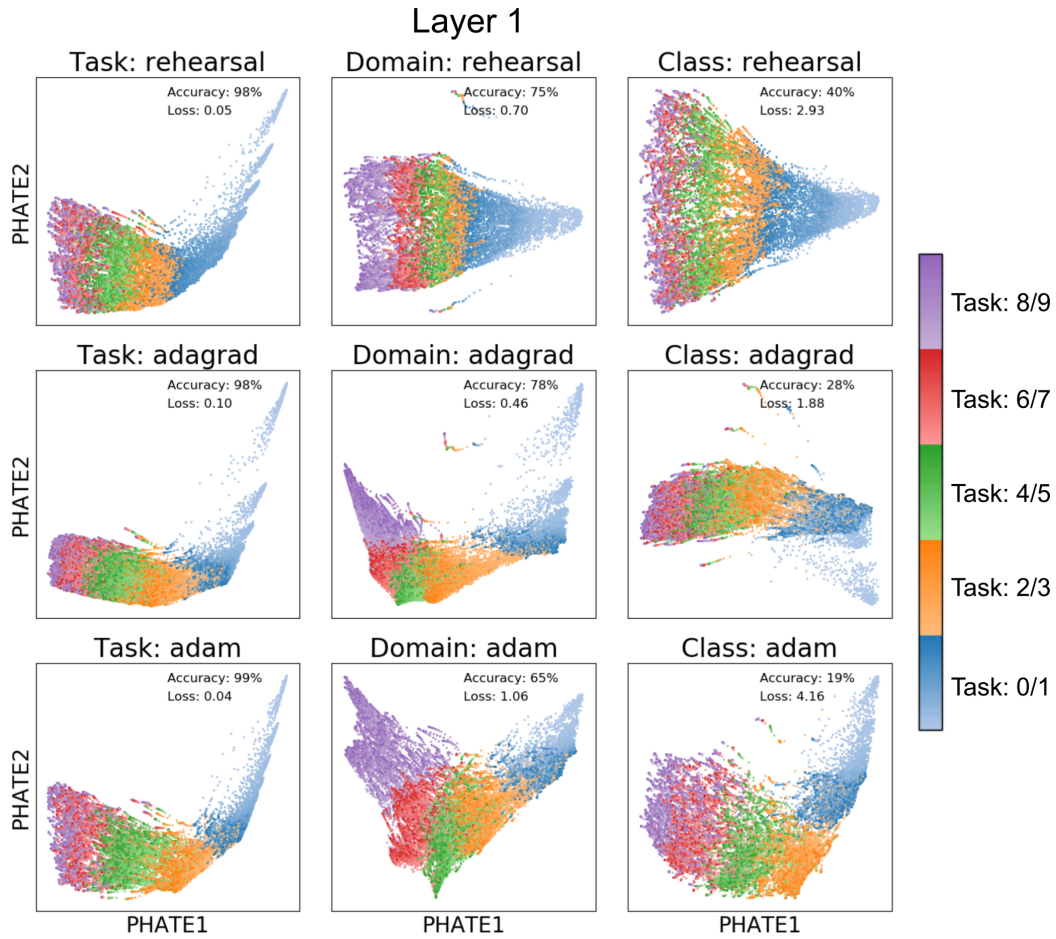


Figure S5: Visualization of layer 1 of a 2 layer MLP trained on Split MNIST for five-task continual learning of binary classification. Accuracy is reported on a test set consisting of an even number of samples from all tasks.

## S7 Computing infrastructure

All computation was done on a single 36-core workstation running Arch Linux with a NVIDIA TITAN X graphics card and 1TB of RAM.



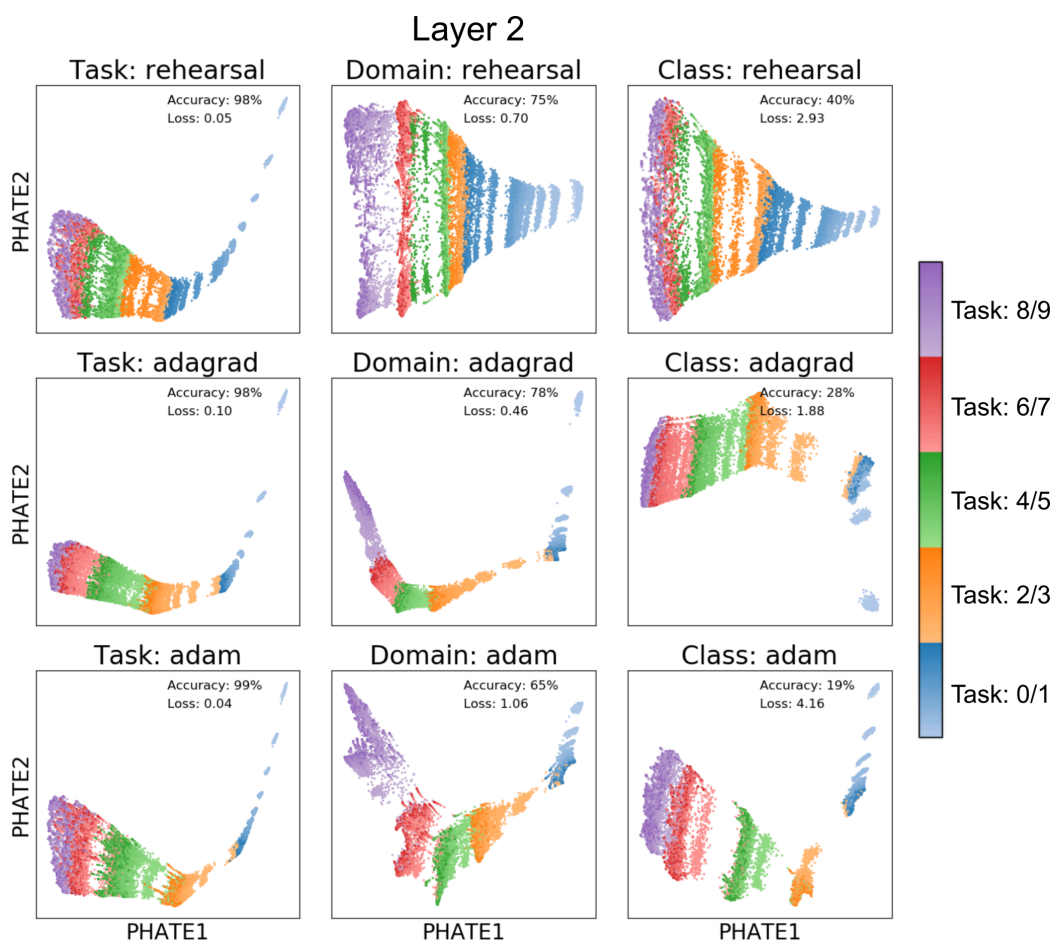


Figure S6: Visualization of layer 2 of a 2 layer MLP trained on Split MNIST for five-task continual learning of binary classification. Accuracy is reported on a test set consisting of an even number of samples from all tasks.